Finite Volume Method for Solving a Modified 3-D 3-Phase Black-Oil Hydrocarbon Secondary Migration Model, and Its Application to the Kuqa Depression of the Tarim Basin in Western China

SHI Guangren[1,*]; MA Jinshan[1]; YANG Xinshe[2]; CHANG Junhua[1]; WAN Jun[1]

[1]Research Institute of Petroleum Exploration and Development, PetroChina, P. O. Box 910, Beijing, 100083, China.
[2]Mathematics and Scientific Computing, National Physical Laboratory, London TW11 0LW, UK
*Corresponding author.
Email: grs@petrochina.com.cn

Abstract

By using a finite volume method as a solver, a modified 3-D 3-phase (water, oil, gas) black-oil model for modeling hydrocarbon (HC) secondary migration in the context of basin modeling is presented in this paper. The model predicts the quantity and distribution of HC accumulation in space and time. The black-oil model used in basin modeling is more complex and more difficult to model than that in reservoir simulations, as the model includes variable simulation ranges, very long simulation times, initial conditions, natural sources and sinks, and reservoir gridcells. In the proposed finite volume formulation, the gridding of variable 3-D geological volumes is performed using perpendicular bisection (PEBI) gridcells, which makes the discretization and subsequent implementation of 3-phase flow equations much easier than when using hexahedral or tetrahedral gridcells. The stability and convergence of the solutions have been improved by using finite volumes with PEBI gridcells and the fully implicit formulation. A detailed case study in the Kuqa Depression of the Tarim Basin in western China shows that the simulation results and predictions agree well with field evaluations.

Key words: Basin modeling; Secondary migration; Black-oil model; Finite volume method; PEBI gridding; Kuqa Depression

INTRODUCTION

The secondary migration of oil and gas, also called hydrocarbon (HC) migration and accumulation, is the most important and yet challenging task in basin modeling. Generally speaking, 1-D (*z*) basin modeling[e.g. 1, 2, 3], which is applicable in less explored areas where there are a few wells drilled, cannot simulate secondary migration. 2-D (*x*-*z*) basin modeling[e.g. 4, 5, 6], applicable in moderately-explored areas where some wells have been drilled and seismic sections do exist, cannot provide the amount of HC accumulated, though it is useful for analyzing secondary migration, and it usually involves two-phase (oil-water) models. 3-D (*x*-*y*-*z*) basin modeling however can simulate secondary migration and is applied in relatively explored areas where more wells have been drilled and seismic coverage is more complete. These 3-D models are mostly two-phase (usually oil-water but sometimes gas-water) models[e.g. 7, 8, 9, 10], and seldomly three-phase (oil-gas-water) models or even compositional models[e.g. 11, 12]. The solver used for the 3-D 3-phase black-oil model for modeling HC secondary migration is the control-volume finite-element method described in detail by Hantschel et al. using hexahedral gridcells[11] and by Mello et al. using tetrahedral gridcells[12], but no detailed examples were given. This paper provides detailed examples of both the finite volume solver using multi-angular prisms with perpendicular bisection (PEBI), and an example to demonstrate its application.

In this paper, a modified 3-D 3-phase (water, oil, gas) black-oil model using the finite volume method for secondary migration is presented. The black-oil model commonly used in reservoir simulations has been modified and introduced into the basin modeling process as a simulator. It is well known that basin modeling is applied to petroleum exploration while reservoir simulation for petroleum production. Though the basic equations (for water, oil and gas) are essentially the same second order parabolic partial differential equations as used in reservoir

simulations, they exhibit eight completely different characteristics (see Table 1). For example, in basin evolution, the natural driving forces are a result of various geological events and HC expulsion, whereas in reservoir simulations these driving forces are man-made. To ensure the validity of the simulation results and the stability and convergence of solutions, special processing procedures are needed with respect to the different conditions shown in Table 1. Therefore, the filtration environment and solutions of basin modeling are much more complicated and difficult to achieve than those of reservoir simulations.

Table 1
Different Characteristics between Basin Modeling and Reservoir Simulation

Characteristic	Basin modeling	Reservoir simulation
Simulation space (x, y, z)	Variable: increasing globally, decreasing or even lost locally	Fixed
Simulation area (x, y)	10^2–10^5 (km^2)	1–10^3 (km^2)
Simulation time	Very long: 10^7–10^9 (years)	Very short: 1–100 (years)
Simulation timestep	0.005–0.1 (million years)	1–30 (days)
Driving forces	Natural forces caused by various geological events in basin evolution	Man-made forces generated by well injection and production
Initial conditions	Single-phase (water)	Water, oil/gas
Sources	Oil/gas expelled from source rocks	Injection into wells
Sinks	Water lost at Earth's surface	Production from wells

1. GRIDDING OF 3-D VARIABLE GEOLOGICAL VOLUME

During the evolution of a basin, the geometrical volume of the basin may increase significantly and globally due to subsidence and deposition; it may be also decrease slightly due to sedimentary compaction. Other factors that may affect the basin volume include hiatuses, undercompaction, erosion, faulting, fracturing, tectonic movements, and paleobathymetry. Hence in basin modeling the geological volume being studied varies with time, in contrast to the fixed volumes used for reservoir simulations. To quantitatively model a basin, the geological volume of a basin must be partitioned into a large number of small grid blocks, called gridcells.

Up to now, there are two types of gridcells widely used for basin partitions: hexahedrons as shown in Fig. 1(a), used mainly in finite difference methods; and tetrahedrons as shown in Fig. 1(b), used primarily in finite element methods. Multi-angular prisms with PEBI as shown in Fig. 1(c) will be used in the finite volume formulation below.
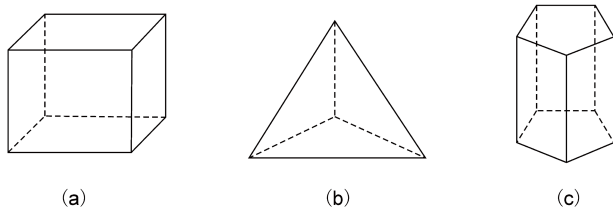
The fundamental ideas of PEBI gridding are perpendicularity and bisection, that is, the line between arbitrary neighboring gridcell centers (e.g. the relation of C_1 to C_2, C_3, C_4 and C_5 shown in Fig. 2) is bisected by their common surface. As shown in Fig. 2, the gridcell V_1 centered at C_1 has four neighboring gridcells, centered at C_2, C_3, C_4 and C_5, respectively. These gridcells are referred to as V_2, V_3, V_4 and V_5, respectively. By taking V_1 and V_2 as an example, the line C_1-C_2 between their centers C_1 and C_2 is perpendicular to their common surface S_1-S_2, and bisected by the surface such that M_{12} is the midpoint of C_1-C_2. The relations between V_1 and V_3, V_4 and V_5 are similar to those between V_1 and V_2. A major advantage of the perpendicularity and bisection method of PEBI gridcells is that it makes the discretization of the finite volume formulation much easier than when using hexahedral or tetrahedral gridcells.

Figure 1
Three Types of Gridcells for Gridding of 3-D Geological Volumes. (a) Hexahedron; (b) Tetrahedron; (c) Multi-angular Prism with Perpendicular Bisection (PEBI)
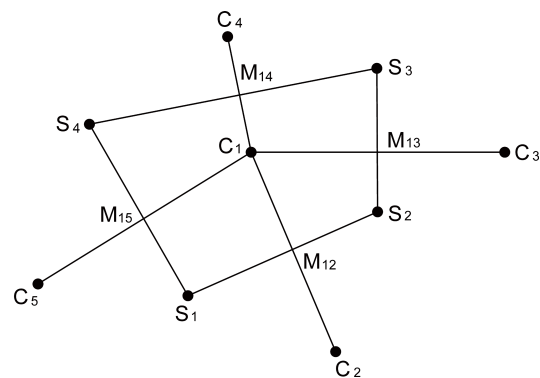

Figure 2
Basic Characteristics of Perpendicular Bisection (PEBI) Gridding

2. A MODIFIED 3-D 3-PHASE BLACK-OIL MODEL

The primary migration of oil and gas, also called HC expulsion, is defined as the movement of generated HC from low porosity and low permeability source rock to its encounter with higher permeability beds. The secondary migration of oil and gas, also called HC migration and accumulation, is the series of oil/gas movements after primary migration through the higher porosity and higher permeability carrier beds. If a suitable reservoir structure is encountered within the range of secondary migration, an oil/gas accumulation may be formed[13]. Therefore, in basin modeling, the HC secondary migration model is run after the execution of geohistory, geothermal history, diagenetic history, HC generation history, and especially HC expulsion history models.

In order to develop an effective way of describing oil/gas secondary migration, a modified 3-D 3-phase black-oil model is now presented.

2.1 Three-Phase Flow Equations

As a starting point the following assumptions or approximations are made: 1) no phase transfers occur between the water and oil; 2) no phase transfers occur between the water and gas; and 3) a one-way phase transfer can occur between the gas and oil, that is, gas moves in and out of the oil, but the oil does not vaporize into the gas phase.

With the above assumptions, the following 3-phase flow partial differential equations (PDE) can be derived by combining the four basic equations of fluid movement (continuity equation, flow potential, Darcy's law, and equations of state)[14]:

Water-phase PDE

$$\nabla \bullet \{a_{\mathrm{w}}(\nabla p_{\mathrm{w}} - \rho_{\mathrm{w}} \mathrm{g} \nabla z)\} \pm Q_{\mathrm{w}} = \partial (\text{\O} S_{\mathrm{w}}/B_{\mathrm{w}})/\partial t, \quad (1)$$

Oil-phase PDE

$$\nabla \bullet \{a_{\mathrm{o}}(\nabla p_{\mathrm{o}} - \rho_{\mathrm{o}} \mathrm{g} \nabla z)\} \pm Q_{\mathrm{o}} = \partial (\text{\O} S_{\mathrm{o}}/B_{\mathrm{o}})/\partial t, \quad (2)$$

Gas-phase PDE

$$\nabla \bullet \{a_{\mathrm{g}}(\nabla p_{\mathrm{g}} - \rho_{\mathrm{g}} \mathrm{g} \nabla z)\} + \nabla \bullet \{a_{\mathrm{o}} R_{\mathrm{s}}(\nabla p_{\mathrm{o}} - \rho_{\mathrm{o}} \mathrm{g} \nabla z)\} \pm (Q_{\mathrm{g}} + R_{\mathrm{s}} Q_{\mathrm{o}}) = \partial [\text{\O}(S_{\mathrm{g}}/B_{\mathrm{g}} + R_{\mathrm{s}} S_{\mathrm{o}}/B_{\mathrm{o}})]/\partial t. \quad (3)$$

These equations form the so-called black-oil model. Let l express arbitrary phase, such that l=w (water), o (oil), or g (gas), respectively. In Eqs. (1)–(3), ∇ is the gradient operator, a_l (units of m^2 $Pa^{-1}s^{-1}$) is the tensor of $a_l = kk_{rl}/(\mu_l B_l)$ where k is the absolute permeability tensor (directional absolute permeability) with units of m^2, k_{rl} is the relative permeability to phase l ($k_{rl} \in [0,1]$), μ_l (units of Pa•s) is the viscosity of phase l, and B_l (with units of m^3/m^3) is the formation volume factor of phase l. In addition, p_l

(Pa) is the pressure in phase l, ρ_l (kg/m^3) is the density of phase l, and g is the gravitational acceleration (m/s^2) and can be taken as 9.81. The burial depth z (in meters) is the thickness of the overlying sediments, Q_l (s^{-1}) is the volumetric source/sink term for phase l, $\text{\O}$ (fraction) is the rock porosity, S_l (fraction) is the saturation of phase l, R_{s} (units of m^3/m^3) is the gas solubility in oil, and t (in seconds) is the time. Since k_{rw} and k_{rg} are functions of S_{w} and S_{g}, respectively, they can be found from the relative permeability functions; k_{ro} can be calculated from the improved Stone formula[14]. Since μ_{w}, μ_{o} and μ_{g} are functions of p_{w}, p_{o} and p_{g} respectively, B_{w}, B_{o} and B_{g} are functions of p_{w}, p_{o} and p_{g}, respectively, and R_{s} is a function of p_{o}, they can be derived from the PVT functions[14].

Mass conservation leads to the saturation-balance equation:

$$S_{\mathrm{w}} + S_{\mathrm{o}} + S_{\mathrm{g}} = 1. \quad (4)$$

Capillary pressures can be expressed as

$$p_{\mathrm{cow}} = p_{\mathrm{o}} - p_{\mathrm{w}}, \quad (5)$$

$$p_{\mathrm{cog}} = p_{\mathrm{g}} - p_{\mathrm{o}}, \quad (6)$$

where p_{cow} (Pa) is the capillary pressure in the oil-water system, and p_{cog} (Pa) is the capillary pressure in the oil-gas system. Since p_{cow} and p_{cog} are functions of S_{w} and S_{g}, respectively, they can be found from the relative permeability functions[14].

When the initial and boundary conditions for a geological volume are given, the six unknowns (p_{w}, p_{o}, p_{g} and S_{w}, S_{o}, S_{g}) in the volume can be calculated by using the six equations (1)–(6). Therefore, the pressure and saturation histories of water, oil and gas are uniquely determined, and describe the basic states of oil/gas secondary migration in the volume.

In calculations for modeling HC secondary migration, the potentials of water, oil and gas (i.e. Φ_{w}, Φ_{o} and Φ_{g} with units of Pa, respectively) are often used, and are given by

$$\Phi_l = p_l - \rho_l \mathrm{g} z \ (l=\mathrm{w, o, g}), \quad (7)$$

and $\rho_{\mathrm{w}} = \rho_{\mathrm{w}0}/B_{\mathrm{w}}, \rho_{\mathrm{o}} = (\rho_{\mathrm{o}0} + R_{\mathrm{s}} \rho_{\mathrm{g}0})/B_{\mathrm{o}}, \rho_{\mathrm{g}} = \rho_{\mathrm{g}0}/B_{\mathrm{g}},$ (8)

where $\rho_{\mathrm{w}0}$, $\rho_{\mathrm{o}0}$ and $\rho_{\mathrm{g}0}$ (kg/m^3) are the densities of water, oil and gas at standard conditions, respectively. $\rho_{\mathrm{w}0}$=997.1, $\rho_{\mathrm{o}0}$=807.8 and $\rho_{\mathrm{g}0}$=1.0365 are used in the case study below.

2.2 Initial Conditions

Initial conditions mainly refer to the initial values of the pressures and saturations of water, oil and gas in the geological volume before secondary migration starts. Usually initial conditions of S_{w}=1, S_{o}=0, S_{g}=0 are used, while $p_{\mathrm{o}} = \rho_{\mathrm{o}} \mathrm{g} z$, p_{w} and p_{g} are determined by Eqs. (5) and

(6), respectively. Moreover, the simulator does not start to run until expelled oil or gas occurs ($Q_o \neq 0$ or $Q_g \neq 0$) in the basin, so as to save simulation time. It is obvious that the initial conditions are different from those in reservoir simulations.

2.3 Boundary Conditions

Letting q_l (m^3/s) be the source/sink term for phase l and V (m^3) be the volume of a PEBI gridcell, we find that $q_l = Q_l \cdot V$. There exist three kinds of boundary conditions: 1) closed boundary at basin boundaries other than the Earth's surface, 2) inflow "boundaries" in the source rock formation where the oil and gas were expelled (these boundaries are treated as "source" $+ q_o$ and $+ q_g$; in this case, the sign "±" in Eqs. (2) and (3) becomes "+"), and 3) outflow boundary at the Earth's surface where water flowed out of the basin (this boundary is considered as "sink" $- q_w$, and thus the sign "±" in Eq. (1) simply becomes "−"). Here the boundaries (2) and (3) are opposite to those used in reservoir simulations. Assuming that the total pore volume in a basin remains approximately constant over short time-intervals, then $\sum_m (q_o + q_g) = \sum_n q_w$ at the gridcells on the flow boundaries, where m is the number of inlets on the inflow boundaries, and n is the number of outlets on the outflow boundaries. Finally, q_w can be approximated by $\frac{1}{n} \sum_m (q_o + q_g)$ since $\mathbf{a}_l$ is almost constant at the Earth's surface.

The Neumann conditions are applied to the closed boundaries:

$$\partial \Phi_l / \partial \mathbf{n} = 0, \partial S_l / \partial \mathbf{n} = 0, (l = w, o, g) \qquad (9)$$

where $\mathbf{n}$ is the external unit normal vector of the boundaries.

2.4 Absolute Permeability

Let k be the absolute permeability (m^2) in the absence of microfracturing/faulting, which can be estimated from porosity using the Kozeny-Carman formula[6, 15] or the porosity-power function[15, 16, 17, 18]. The Kozeny-Carman formula is chosen in the case study since it relies on the specific surface area of the solid matrix for each different rock type. Two special procedures for dealing with microfractures and faults are discussed below.

Let p_f (Pa) be the fluid pressure, p_{od} (Pa) be the total load of the overlying deposits, k_s (m^2) be the permeability of sandstone, and k_f (m^2) be the permeability in the existence of microfracturing. If $p_f < C_f \cdot p_{od}$ where $C_f \in [0.8, 0.9]$, no microfracturing occurs so that $k_f = k$; if $p_f \geq C_f \cdot p_{od}$, microfracturing occurs so that $k_f = k + k_s (1 - C_f p_{od} / p_f)^2$ [19]. $C_f = 0.85$ is used as a default value.

The permeability of fault zones can be calculated by specific modeling approaches[e.g. 20, 21, 22, 23, 24]. Permeability enhancements of nearly one order of magnitude (relative to the host rock) are observed for the fault-parallel component in some regions. Fault-normal permeability, by contrast, may be two orders of magnitude less than the host rock permeability[23].

2.5 Reservoir Gridcells

A reservoir body should consist of sufficient and qualified reservoir rocks. Generally speaking, reservoir rocks are classified into two major types, namely, clastic rocks and carbonate rocks, i.e. sandstone and limestone. It is necessary to determine whether each gridcell is a reservoir gridcell or not. The three categories used to determine if a gridcell is a reservoir gridcell are: 1) if the sandstone content of part of a gridcell is larger than a specified threshold (e.g. 50%), this gridcell can be defined as a potential oil/gas reservoir gridcell; 2) there is no such threshold for classifying reservoir limestone, instead limestone gridcells are selected as potential oil/gas reservoir gridcells on the basis of favorable sedimentary facies, diagenesis and structural fracturing; and 3) all other gridcells are classified as non-reservoir gridcells. In calculating the amount of oil/gas accumulated, the results can be divided into two classes: 1) oil/gas in reservoir gridcells, which classification represents true oil/gas accumulations; and 2) oil/gas in non-reservoir gridcells, which is characteristic of oil/gas lost along migration pathways. These classifications are again different from those used in reservoir simulations.

3. FINITE VOLUME FORMULATION WITH PEBI GRIDDING

3.1 Finite Volume Equations

The 3-phase coupled flow equations (1)–(3) are partial differential equations which are too complicated to be solved analytically for geologically realistic models. Up to now, there are three major types of approximations to the equations: finite difference, finite element, and finite volume. The finite volume method, which is similar in many ways to the finite difference method, is very flexible in dealing with irregular geometries and various boundary conditions with various types of gridcells, and many studies have shown its advantages in the application of reservoir simulations[25, 26, 27, 28].

The finite volume formulation is derived from the integral median theorem and the Gauss divergence theorem:

$$\iiint_v \text{div}(\mathbf{u}) \, \mathrm{d}v = \oiint_s \mathbf{u} \cdot \mathbf{n} \, \mathrm{d}s \qquad (10)$$

where div denotes the divergence of a vector field $\mathbf{u}$, v is an arbitrary finite volume, s is the surface of v, and $\mathbf{n}$ is the external unit normal vector of the surface s.

Let v_i ($i = 1, 2, \ldots, I$ where I is the number of gridcells) be a gridcell generated by PEBI gridding, and s_{ij} ($j = 1, 2, \ldots, J_i$ where J_i is the number of surfaces of v_i) be a surface of v_i (for example, $J_i = 7$ in the specific sample illustrated in Fig. 1(c)). Using Eq. (7) and integrating over v_i on both

sides of Eqs. (1)–(3) respectively, the following integral equations are obtained:

$$\oiiint_{v_i}\{\mathrm{div}(\boldsymbol{a}_\mathrm{w}\,\mathrm{grad}(\varPhi_\mathrm{w}))-Q_\mathrm{w}\}\,\mathrm{d}v=\oiiint_{v_i}[\partial(\phi S_\mathrm{w}/B_\mathrm{w})/\partial t]\,\mathrm{d}v \quad (11)$$

$$\oiiint_{v_i}\{\mathrm{div}(\boldsymbol{a}_\mathrm{o}\,\mathrm{grad}(\varPhi_\mathrm{o}))+Q_\mathrm{o}\}\,\mathrm{d}v=\oiiint_{v_i}[\partial(\phi S_\mathrm{o}/B_\mathrm{o})/\partial t]\,\mathrm{d}v \quad (12)$$

$$\oiiint_{v_i}\{\mathrm{div}(\boldsymbol{a}_\mathrm{g}\,\mathrm{grad}(\varPhi_\mathrm{g}))+\mathrm{div}(\boldsymbol{a}_\mathrm{o}R_\mathrm{s}\,\mathrm{grad}(\varPhi_\mathrm{o}))+(Q_\mathrm{g}+R_\mathrm{s}Q_\mathrm{o})\}\,\mathrm{d}v=$$
$$\oiiint_{v_i}\{\partial[\phi(S_\mathrm{g}/B_\mathrm{g}+R_\mathrm{s}S_\mathrm{o}/B_\mathrm{o})]/\partial t\}\,\mathrm{d}v \quad (13)$$

where grad is the gradient of a vector field.

Applying the median theorem and discretizing the right-hand sides of Eqs. (11)–(13), we find

$$[\partial(\phi S_\mathrm{w}/B_\mathrm{w})/\partial t]\big|_\xi\cdot V_i=V_i\cdot\{[(\phi S_{\mathrm{w},i}/B_{\mathrm{w},i})^{n+1}-(\phi S_{\mathrm{w},i}/B_{\mathrm{w},i})^n]/\Delta t\} \quad (14)$$

$$[\partial(\phi S_\mathrm{o}/B_\mathrm{o})/\partial t]\big|_\xi\cdot V_i=V_i\cdot\{[(\phi S_{\mathrm{o},i}/B_{\mathrm{o},i})^{n+1}-(\phi S_{\mathrm{o},i}/B_{\mathrm{o},i})^n]/\Delta t\} \quad (15)$$

$$\{\partial[\phi(S_\mathrm{g}/B_\mathrm{g}+R_\mathrm{s}S_\mathrm{o}/B_\mathrm{o})]/\partial t\}\big|_\xi\cdot V_i=$$
$$V_i\cdot\{[\phi(S_{\mathrm{g},i}/B_{\mathrm{g},i}+R_{\mathrm{s}_i}S_{\mathrm{o},i}/B_{\mathrm{o},i})]^{n+1}-[\phi(S_{\mathrm{g},i}/B_{\mathrm{g},i}+R_{\mathrm{s}_i}S_{\mathrm{o},i}/B_{\mathrm{o},i})]^n\}/\Delta t \quad (16)$$

where t_1 is the start time only when $Q_\mathrm{o}\neq0$ or $Q_\mathrm{g}\neq0$, t_n is the nth time, t_{n+1} is the $(n+1)^\mathrm{th}$ time, and Δt (in seconds) is the nth timestep, and $\Delta t=t_{n+1}-t_n$. V_i (m³) is the volume of the ith gridcell v_i, which is the product of the top or bottom area and the height of the prism gridcell shown in Fig. 1(c).

From the volume integral principle, the second terms on the left-hand sides of Eqs. (11) and (12) as well as the third term on the left-hand side of Eq. (13) can be rewritten as

$$\oiiint_{v_i}Q_\mathrm{w}\,\mathrm{d}v=Q_\mathrm{w}\cdot V_i=q_{\mathrm{w},i} \quad (17)$$

$$\oiiint_{v_i}Q_\mathrm{o}\,\mathrm{d}v=Q_\mathrm{o}\cdot V_i=q_{\mathrm{o},i}, \quad (18)$$

$$\oiiint_{v_i}(Q_\mathrm{g}+R_\mathrm{s}Q_\mathrm{o})\,\mathrm{d}v=(Q_\mathrm{g}+R_\mathrm{s}Q_\mathrm{o})\cdot V_i=q_{\mathrm{g},i}+R_{\mathrm{s}_i}q_{\mathrm{o},i} \quad (19)$$

Applying the Gauss divergence theorem to the first terms on the left-hand sides of both Eqs. (11) and (12) as well as the first and second terms on the left-hand side of Eq. (13), we find

$$\oiiint_{v_i}\{\mathrm{div}(\boldsymbol{a}_\mathrm{w}\,\mathrm{grad}(\varPhi_\mathrm{w}))\}\,\mathrm{d}v=\sum_{j=1}^{J_i}\oiint_{s_{ij}}(\boldsymbol{a}_\mathrm{w}\,\mathrm{grad}(\varPhi_\mathrm{w}))\cdot\boldsymbol{n}\,\mathrm{d}s=\sum_{j=1}^{J_i}\oiint_{s_{ij}}a_{\mathrm{w},n}\cdot(\partial\varPhi_\mathrm{w}/\partial\boldsymbol{n})\,\mathrm{d}s \quad (20)$$

$$\oiiint_{v_i}\{\mathrm{div}(\boldsymbol{a}_\mathrm{o}\,\mathrm{grad}(\varPhi_\mathrm{o}))\}\,\mathrm{d}v=\sum_{j=1}^{J_i}\oiint_{s_{ij}}(\boldsymbol{a}_\mathrm{o}\,\mathrm{grad}(\varPhi_\mathrm{o}))\cdot\boldsymbol{n}\,\mathrm{d}s=\sum_{j=1}^{J_i}\oiint_{s_{ij}}a_{\mathrm{o},n}\cdot(\partial\varPhi_\mathrm{o}/\partial\boldsymbol{n})\,\mathrm{d}s \quad (21)$$

$$\oiiint_{v_i}\{\mathrm{div}(\boldsymbol{a}_\mathrm{g}\,\mathrm{grad}(\varPhi_\mathrm{g}))+\mathrm{div}(\boldsymbol{a}_\mathrm{o}R_\mathrm{s}\,\mathrm{grad}(\varPhi_\mathrm{o}))\}\,\mathrm{d}v=\sum_{i=1}^{J_i}\oiint_{s_{ij}}\{\boldsymbol{a}_\mathrm{g}\,\mathrm{grad}(\varPhi_\mathrm{g})+\boldsymbol{a}_\mathrm{o}R_\mathrm{s}\,\mathrm{grad}(\varPhi_\mathrm{o})\}$$
$$\cdot\boldsymbol{n}\,\mathrm{d}s=\sum_{j=1}^{J_i}\oiint_{s_{ij}}\{a_{\mathrm{g},n}\cdot(\partial\varPhi_\mathrm{g}/\partial\boldsymbol{n})+a_{\mathrm{o},n}R_\mathrm{s}\cdot(\partial\varPhi_\mathrm{o}/\partial\boldsymbol{n})\}\,\mathrm{d}s \quad (22)$$

where $a_{l,n}$ is the projection of tensor $\boldsymbol{a}_l$ in the $\boldsymbol{n}$ direction, and $\boldsymbol{n}$ is the external unit normal vector of the surface s_{ij} of v_i.

In order to label the neighborhood gridcells surrounding a given gridcell v_i in a coherent way, $N(i,j)$ is used to denote the neighbor gridcell corresponding the jth surface s_{ij} of v_i. For example, for the gridcell $i=1610$ with 8 surfaces (thus $J_{1610}=8$), the neighboring gridcells are 1609, 1611, …, 10 and 3210, and therefore $N(1610,1)=1609$, $N(1610,2)=1611$, …, $N(1610,7)=10$ and $N(1610,8)=3210$.

From the median theorem,

$$\oiint_{s_{ij}}a_{l,\mathrm{n}}\cdot(\partial\varPhi_l/\partial\boldsymbol{n})\,\mathrm{d}s=[a_{l,\mathrm{n}}\cdot(\partial\varPhi_l/\partial\boldsymbol{n})]\big|_{B(i,j)}\cdot S_{ij}\quad(l=\mathrm{w,\,o,\,g})\quad(23)$$

where $B(i,j)$ is the midpoint on the line linking the center of gridcell v_i and the center of the neighboring gridcell $v_{N(i,j)}$, which is located on the intersecting surface s_{ij} between v_i and $v_{N(i,j)}$; and S_{ij} (m²) is the area of the intersecting surface s_{ij} (see Fig. 2).

Since the line linking the centers of two adjacent gridcells is normal to the common surface s_{ij} of the two gridcells, and using ΔL (in meters) to denote the length of this line (see Fig. 2) and using the discretization, the above equation can be written as

$$\oiint_{s_{ij}}a_{l,\mathrm{n}}\cdot(\partial\varPhi_l/\partial\boldsymbol{n})\,\mathrm{d}s=a_{l,\mathrm{n}}(B(i,j))\cdot[(\varPhi_{l,n(i,j)}-\varPhi_{l,i})/\Delta L]\cdot S_{ij}\quad(l=\mathrm{w,\,o,\,g})\quad(24)$$

From Eq. (24), the multiple integrals in Eqs. (20)–(22) can be written as

$$\oiiint_{v_i}\{\mathrm{div}(a_i\,\mathrm{grad}(\varPhi_i))\}\,\mathrm{d}v=\sum_{j=1}^{J_i}\{a_{l,\mathrm{n}}(B(i,j))\cdot[(\varPhi_{l,n(i,j)}-\varPhi_{l,i})/\Delta L]\cdot S_{ij}\}\quad(l=\mathrm{w,\,o,\,g})\quad(25)$$

$$\oiiint_{v_i}\{\mathrm{div}(a_\mathrm{o}R_\mathrm{s}\,\mathrm{grad}(\varPhi_\mathrm{o}))\}\,\mathrm{d}v=\sum_{j=1}^{J_i}\{a_{\mathrm{o},\mathrm{n}}R_\mathrm{s}(B(i,j))\cdot[(\varPhi_{\mathrm{o},n(i,j)}-\varPhi_{\mathrm{o},i})/\Delta L]\cdot S_{ij}\}\quad(26)$$

From Eqs. (14)–(19) and (25)–(26), (11)–(13) can be discretized as

Discretized equation of water-phase

$$\sum_{j=1}^{J_i}\{a_{\mathrm{w},\mathrm{n}}(B(i,j))\cdot[(\varPhi_{\mathrm{w},n(i,j)}^{n+1}-\varPhi_{\mathrm{w},i}^{n+1})/\Delta L]\cdot S_{ij}\}-q_{\mathrm{w},i}^{n+1}=$$
$$V_i\cdot\{[(\phi S_{\mathrm{w},i}/B_{\mathrm{w},i})^{n+1}-(\phi S_{\mathrm{w},i}/B_{\mathrm{w},i})^n]/\Delta t\} \quad (27)$$

Discretized equation of oil-phase

$$\sum_{j=1}^{J_i}\{a_{\mathrm{o},\mathrm{n}}(B(i,j))\cdot[(\varPhi_{\mathrm{o},n(i,j)}^{n+1}-\varPhi_{\mathrm{o},i}^{n+1})/\Delta L]\cdot S_{ij}\}+q_{\mathrm{o},i}^{n+1}=$$
$$V_i\cdot\{[(\phi S_{\mathrm{o},i}/B_{\mathrm{o},i})^{n+1}-(\phi S_{\mathrm{o},i}/B_{\mathrm{o},i})^n]/\Delta t\} \quad (28)$$

Discretized equation of gas-phase

$$\sum_{j=1}^{J_i}[\{a_{\mathrm{g},\mathrm{n}}(B(i,j))\cdot[(\varPhi_{\mathrm{g},n(i,j)}^{n+1}-\varPhi_{\mathrm{g},i}^{n+1})/\Delta L]+a_{\mathrm{o},\mathrm{n}}R_\mathrm{s}(B(i,j))\cdot[(\varPhi_{\mathrm{o},n(i,j)}^{n+1}-\varPhi_{\mathrm{o},i}^{n+1})/\Delta L]\}\cdot S_{ij}]+$$
$$(q_{\mathrm{g},i}^{n+1}+R_{\mathrm{s}_i}^{n+1}q_{\mathrm{o},i}^{n+1})=V_i\cdot\{[\phi(S_{\mathrm{g},i}/B_{\mathrm{g},i}+R_{\mathrm{s}_i}S_{\mathrm{o},i}/B_{\mathrm{o},i})]^{n+1}-[\phi(S_{\mathrm{g},i}/B_{\mathrm{g},i}+R_{\mathrm{s}_i}S_{\mathrm{o},i}/B_{\mathrm{o},i})]^n\}/\Delta t \quad (29)$$

In Eqs. (27)–(29), $a_{l,n}(B(i,j))$ is the projection of $\boldsymbol{a}_l(B(i,j))$ in the direction of normal $\boldsymbol{n}$. Letting k_n (m²) be the projection of tensor $\boldsymbol{k}$ in the direction of normal $\boldsymbol{n}$, and

using $a_l=kk_{rl}/(\mu_l B_l)$,

$$a_{l,n}(B(i,j))= [k_n k_{rl}/(\mu_l B_l)]|_{B(i,j)} \quad (l=\text{w, o, g}) \qquad (30)$$

where k_n can be expressed as

$$k_n=k_x k_y k_z (k_y^2 k_z^2 \cos^2\alpha+k_x^2 k_z^2 \cos^2\beta+k_x^2 k_y^2 \cos^2\gamma)^{-0.5} \qquad (31)$$

where the rule of ellipsoid is used; α, β and γ (degrees) are the angles between $\mathbf{n}$ and x, y and z (in meters) respectively; $(\cos\alpha, \cos\beta, \cos\gamma)$ are the components of the unit vector $\mathbf{n}$; and k_x, k_y and k_z (m^2) are the absolute permeabilities of $\mathbf{k}$ in the direction of the x, y and z axes, respectively, as determined by

$$k_x=\lambda_x k, \, k_y=\lambda_y k, \, k_z=\lambda_z k, \qquad (32)$$

where k is discussed in Subsection 3.4; the values of λ_x, λ_y and λ_z depend on the heterogeneous nature of rock formations and their petrophysical properties, usually $\lambda_x \approx 1$, $\lambda_y \approx 1$, but λ_z can vary within the range of 0.01–1.

3.2 Fully Implicit Formulation

Though the IMPES (i.e. implicit pressure and explicit saturation) formulation is simple and easy for calculations, the IMPES formulation produces unrealistic results which are potentially caused by the use of incorrect saturations. In order to ensure stability and convergence, the full implicit scheme for the solution of the nonlinear equations (27)–(29) is used. The fully implicit formulation involves implicit pressure and implicit saturation, using the Newton iteration method with a superlinear convergence rate and a relatively sparse matrix. This is well-known in reservoir simulations[29], and required for basin modeling since its solution is much more accurate, as well as being much more complicated and difficult than the former (see Table 1).

Now there are six unknowns: S_w, S_g and P_o [which can be solved from Eqs. (27)–(29)], and S_o, P_w and P_g [determined from Eqs. (4)–(6)]. Suppose modeling has reached the nth timestep. Letting $\mathbf{x}^n$ and $\mathbf{x}^{n+1}$ be the vector (S_w, S_g, P_o) at the nth and $(n+1)^{th}$ time, respectively, $\mathbf{x}^{n+1}$ can be then obtained by solving from $\mathbf{x}^n$

$$F(\mathbf{x}^{n+1})= \begin{cases} R_w = 0 \\ R_o = 0 \\ R_g = 0 \end{cases} \qquad (33)$$

where $\mathbf{F}$ is the nonlinear vector in terms of the unknown vector $\mathbf{x}^{n+1}$. R_w, R_o and R_g are the residuals which are the difference between the right-hand sides and the left-hand sides of Eqs. (27)–(29), respectively. The basic steps of the Newton iteration are as follows: letting $\mathbf{x}$ be the solution of Eq. (33) at the kth iteration and $\delta\mathbf{x}(k)=\mathbf{x}(k+1)-\mathbf{x}(k)$ be its correction, substituting $\delta\mathbf{x}(k)=\mathbf{x}(k+1)-\mathbf{x}(k)$ in Eq. (33)

and then expanding it in Taylor series and neglecting high-order terms,

$$\mathbf{J}_{(k)}\delta\mathbf{x}(k)=-\mathbf{F}(\delta\mathbf{x}(k)) \qquad (34)$$

where $\mathbf{J}_{(k)}$ is the Jacobi matrix at the kth Newton iteration, that is

$$\mathbf{J}_{(k)}= \begin{bmatrix} \dfrac{\partial R_w}{\partial S_w} & \dfrac{\partial R_w}{\partial S_g} & \dfrac{\partial R_w}{\partial P_o} \\ \dfrac{\partial R_o}{\partial S_w} & \dfrac{\partial R_o}{\partial S_g} & \dfrac{\partial R_o}{\partial P_o} \\ \dfrac{\partial R_g}{\partial S_w} & \dfrac{\partial R_g}{\partial S_g} & \dfrac{\partial R_g}{\partial P_o} \end{bmatrix} \qquad (35)$$

Using the Jacobian equation (35) on each gridcell of the 3-D geological volume, a matrix equation is obtained:

$$\mathbf{AX}=\mathbf{B} \qquad (36)$$

where $\mathbf{A}$ is the $3I\times3I$ coefficient matrix, constructed with I^2 submatrices and each submatrice is a 3×3 matrix. There exist I diagonal sub-matrices, $\sum_i J_i$ non-diagonal nonzero sub-matrices and $(I^2-I-\sum_i J_i)$ non-diagonal zero sub-matrices. $\mathbf{X}$ is the $3I\times1$ unknown column matrix, consisting of $3I$ unknowns (δS_{w1}, δS_{g1}, δp_{o1}, δS_{w2}, δS_{g2}, δp_{o2}, …, δS_{wI}, δS_{gI}, δp_{oI}), and $\mathbf{B}$ is the $3I\times1$ constant column matrix, containing $3I$ residuals (R_{w1}, R_{o1}, R_{g1}, R_{w2}, R_{o2}, R_{g2}, …, R_{wI}, R_{oI}, R_{gI}).

Equation (36) is a nonlinear equation with respect to $3I$ unknowns where $\mathbf{A}$ is a large, sparse and unsymmetrical matrix. This large sparse system can be efficiently solved by the orthogonal minimum residual (ORTHOMIN) algorithm[30] with an incomplete lower-upper (ILU) preconditioner for faster inner iteration convergence rates.

The solution of Eq. (36) is updated based on the following residual convergence criteria:

$$\max\{R_{w1}, R_{o1}, R_{g1}, R_{w2}, R_{o2}, R_{g2}, …, R_{wI}, R_{oI}, R_{gI}\}\leq\varepsilon \qquad (37)$$

at the kth Newton iteration where ε is a pre-specified tolerant error which is assigned to 10 in the case study below. If Eq. (37) is met, and the mass balances is satisfied, then the Newton iteration stops (i.e. the simulation on the nth timestep ends) and thus it can start on the $(n+1)^{th}$ timestep.

3.3 Determination of Parameters at $B(i,j)$

In Eq. (36), the calculations require the values of some parameters at the point $B(i,j)$. However, these values exist only at gridcell centers rather than at $B(i,j)$. Generally speaking, a parameter value at $B(i,j)$ can be taken as the arithmetic mean of the values at the gridcell center and its neighboring gridcell centers, which will be demonstrated by Eqs. (38) and (39) below as examples. But the absolute permeability value at $B(i,j)$ is preferably given by the harmonic mean, as demonstrated below for Eq. (40). Moreover, experimental data suggest that the values of

k_{rw}, k_{ro}, k_{rg}, k'_{rw}, k'_{ro}, k'_{rg}, R_s, R'_s, p_o, S_w and S_g should be determined by the upstream process shown for Eqs. (41)–(43) as an example below[31].

$$\mu_l|_{B(i,j)} = (\mu_l|_i + \mu_l|_{n(i,j)})/2 \quad (l=\text{w, o, g}) \qquad (38)$$

$$B_l|_{B(i,j)} = (B_l|_i + B_l|_{n(i,j)})/2 \quad (l=\text{w, o, g}) \qquad (39)$$

The values of k_x, k_y and k_z in Eq. (32) at $B(i,j)$ should be determined by

$$k_c|_{B(i,j)} = 2k_c|_i \cdot k_c|_{n(i,j)}/(k_c|_i + k_c|_{n(i,j)}) \quad (c=\text{x, y, z}) \qquad (40)$$

$$k_{rl}|_{B(i,j)} = \omega k_{rl}|_i + (1-\omega)k_{rl}|_{n(i,j)} \quad (l=\text{w, o, g}) \qquad (41)$$

$$R_S|_{B(i,j)} = \omega R_S|_i + (1-\omega)R_S|_{n(i,j)}, \quad R'_S|_{B(i,j)} = \omega R'_S|_i + (1-\omega)R'_S|_{n(i,j)} \qquad (42)$$

where

$$\omega = \begin{cases} 1 & \text{when } \Phi_{l,i} > \Phi_{l,n(i,j)} \\ 0.5 & \text{when } \Phi_{l,i} = \Phi_{l,n(i,j)} \quad (l=\text{w, o, g}) \\ 0 & \text{when } \Phi_{l,i} < \Phi_{l,n(i,j)} \end{cases} \qquad (43)$$

and ω in Eq. (42) is determined only by Φ_o.

3.4 Special Procedure for Initialization

When Eq. (36) is solved at t_n, the data in the 3-D geological volume at t_n are known. The next step is to solve Eq. (36) at t_{n+1}, but initial data in the volume at t_{n+1} are unknown since the volumes are different at t_n and t_{n+1}. Here is how to initialize the data in the volume at t_{n+1}: 1) for the added new gridcells due to basin evolution from t_n to t_{n+1}, S_l and p_l can be given by the initial conditions mentioned above; and 2) for other gridcells, the values of S_l and p_o are taken as the same values as those at the nearest gridcell in the same formation in the volume at t_n, but p_o should be increased by $\rho_o g(z_2-z_1)$ where z_1 and z_2 are the burial depths at the corresponding gridcells in the volumes at t_n and t_{n+1}, respectively.

4. CASE STUDY: THE KUQA DEPRESSION

4.1 Petroleum-Geological Setting

Located to the north of the Tarim Basin in western China, the Kuqa Depression covers about 40,000 km², stretching from the mountainous southern Tianshan fold belt in the north to the Tabei uplift in the south (see Fig. 3). It is about 400 km long (E-W) and 50–140 km wide (N-S), wide to the west and narrowing to the east. Formations encountered in the depression consist of Q (Quaternary), N_2k (upper Neogene), $N_{1-2}k$ (middle Neogene), N_1j (lower Neogene), E (Paleogene), K (Cretaceous), J (Jurassic) and T (Triassic) from top to bottom, which have geological ages of 2, 5, 9, 24, 65, 135, 208 and 250 Ma (million

years), respectively. The major source rocks of the depression are middle and lower Jurassic lake-swamp coals, and upper and middle Triassic lacustrine mudstones. The good quality of source rocks and cap rocks, including good Paleogene and Cretaceous sandstone reservoirs beneath the regional cap rock, allowed the oil and gas in the depression to charge mainly vertically from the source rock area to reservoirs in the large gas fields like Kela2 and Dabei etc. This also allowed major lateral migration of oil and gas to form medium-sized condensate oil/gas fields such as Yaha, Yingmai7 and Yangtake in the southern depression 20–30 km away from the source rock area (see Fig. 3). Among the 102 exploration wells drilled in the depression, two wells intersected commercial oil and 56 wells commercial gas[32].
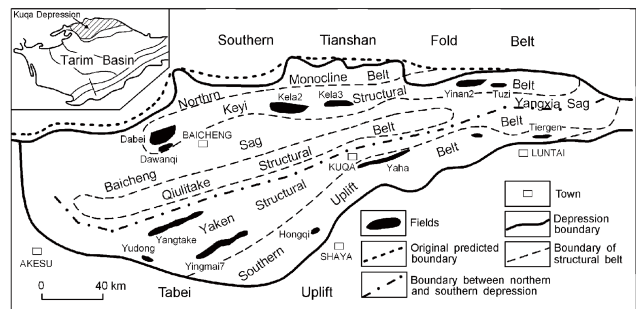

Figure 3
Structures and Reservoirs in the Kuqa Depression (modified from [32])

4.2 Calculation Procedure

In this case study about 90,000 points of data, from 102 drilled wells and 577 pseudo wells taken from seismic sections, were used as input data for the executions of geohistory, geothermal history, diagenetic history, HC generation history, and especially HC expulsion history models[33]. In the geohistory model, the combination of backstripping and overpressure[5, 15, 34] was the main technique used. In the geothermal history model, an inversion of geothermics by using vitrinite reflectance Ro data as a constraint[5, 35, 36] was used. In the diagenetic history model, a simplified dissolution-precipitation model of the smectite to illite transformation[37] was used. In the HC generation history model, the oil and gas generation from kerogen and oil-gas cracking were considered[5, 38, 39]. In the HC expulsion history model, the oil and gas expelled from source rocks were also simulated[5, 33, 40, 41, 42, 43, 44]. The simulation results of the above five models distributed throughout a 3-D geological volume were used as input data of the modified 3-D 3-phase black-oil model described above.

Black-oil modeling is a forward deduction modeling to restore the oil and gas migration-accumulation history from past to present (e.g. from 208 to 0 Ma in the Kuqa Depression). In most cases, the maximum burial depth

of a basin (z_{max}) occurs at 0 Ma (at the present day), and the number of gridcells in the 3-D geological volume (N_{cell}) increases over basin evolution, so N_{cell} also reaches a maximum in the present day. For gridding the 3-D geological volume for the depression, the number of gridcells at the top of 3-D volume is 809, and Δz=100 m. At present, z_{max}=10.8 km, N_{cell}=56,294, and so $\boldsymbol{A}$ in Eq. (36) is 168,882×168,882. The oil and gas were generated and expelled from the two source rock formations J and T, which form the "sources" q_o and q_g in Eqs. (28) and (29), while the oil and gas might have accumulated in any of the formations from Q to T in the depression. There are 4,066 inlets (q_o and q_g) and 5,787 outlets (q_w) at present. Figs. 4(a) and 4(b) illustrate the gridding of the 3-D geological volume of the depression at geological times 24 and 0 Ma, and contain 4 formations (E, K, J and T) and 8 formations (Q, N_2k, $N_{1-2}k$, N_1j, E, K, J and T) respectively, as samples. In the history simulations, the timestep Δt is chosen as 0.025 Ma, and the maximum number of iterations for the Newton and ORTHOMIN methods are chosen as 10 and 50, respectively, to ensure stability and convergence for solving Eq. (36).
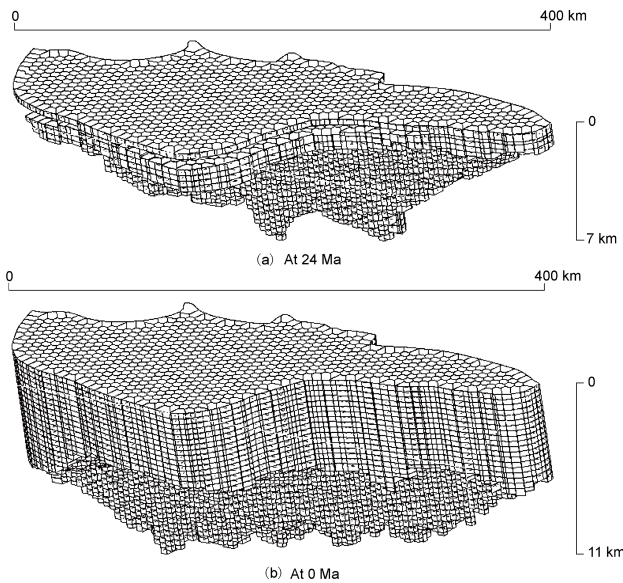
Figure 4
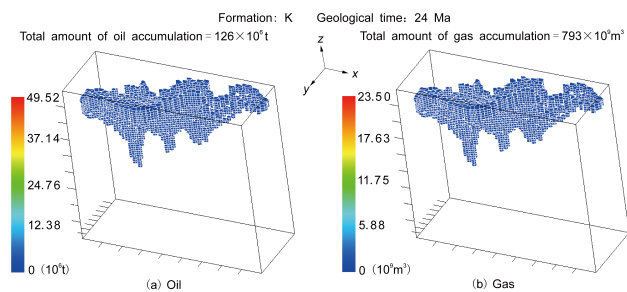**Gridding of the 3-D Geological Volume of the Kuqa Depression at 24 Ma and 0 Ma**

Figure 5
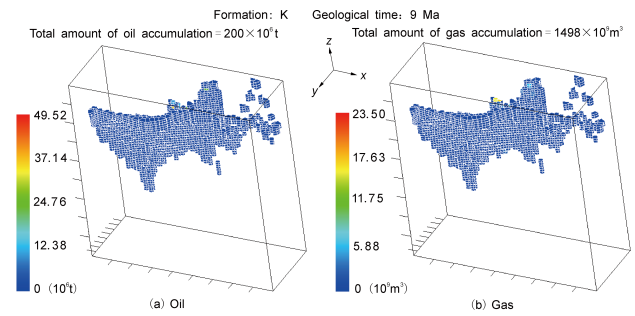**Cumulative Oil and Gas Accumulations in the Cretaceous (K) at 24 Ma**

Figure 6
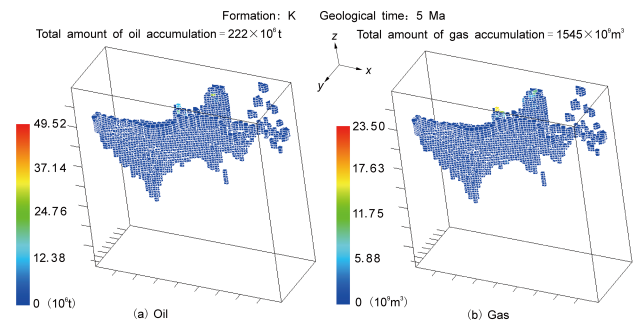**Cumulative Oil and Gas Accumulations in the Cretaceous (K) at 9 Ma**

Figure 7
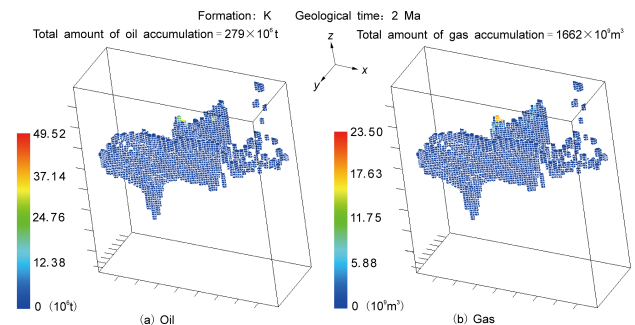**Cumulative Oil and Gas Accumulations in the Cretaceous (K) at 5 Ma**

Figure 8
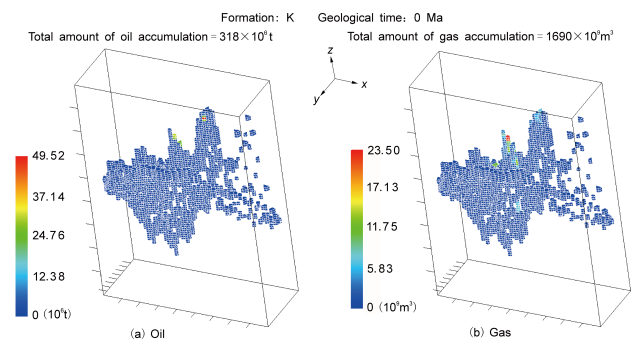**Cumulative Oil and Gas Accumulations in the Cretaceous (K) at 2 Ma**

Figure 9
Cumulative Oil and Gas Accumulations in the Cretaceous (K) at 0 Ma (at present)

4.3 Simulation Results

Using the simulation results of the black-oil model, the oil and gas migration-accumulation histories of each related formation, several conjunctive formations and the whole depression can be shown in 3-D or other forms. For instance, K contains the biggest oil and gas reservoirs, and Figs. 5, 6, 7, 8 and 9 illustrate in 3D the cumulative oil and gas accumulations in the Cretaceous (K) at geological times 24, 9, 5, 2 and 0, respectively.

4.4 Geological Analyses

By comparing the modeled outcomes with actual exploration results, we have made the following four findings.

a. *The Total Amount of Modeled Accumulations in The Whole Depression Agrees with Actual Exploration Results*: The comparisons of the accumulations predicted by modeling with real exploration results are summarized in Table 2. It can be seen from Table 2 that: 1) the ratios of oil and gas expelled to generated are 46.9% and 95.6%, respectively, and the ratios of oil and gas accumulated to expelled are 3.0% and 1.2%, respectively. These values agree with the pool-forming pattern in western China[45, 46]; 2) the total amount of gas accumulated is about 5.8 times larger than that of oil accumulated by both modeling and resource assessment, proving that Kuqa is a gas-rich depression, where 1 tonne of oil is equivalent to 960 m^3 of gas; 3) the residuals of 7.9% for oil and 9.5% for gas between the modeled results and real exploration results indicate the simulation results are reasonably good; and 4) the modeled oil and gas accumulations are larger than the reserves in place, indicating the further prospectivity of exploration.

Table 2
The Total Amounts of Modeled Hydrocarbons Generated, Expelled, and Accumulated, and Reserves in Place by Resource Assessment in the Kuqa Depression

		Oil (10^9 t)	Gas (10^{12} m^3)
Modeled	Generation	29.4	202.6
	Expulsion	13.8	193.6
	Accumulation	0.41	2.3
	Reserves in place by the recent resource assessment	0.38	2.1
	Absolute relative residuals between modeled accumulation and reserves in place (%)	7.9	9.5

b. *The Total Amount of Modeled Accumulations in Each Related Formation Agrees with Actual Exploration Results*: Fig. 10(a) shows modeled oil accumulation data indicating: 1) there is no oil in the upper Tertiary (N_1j, $N_{1-2}k$, N_2k), and only a little oil in the lower Tertiary (E); but 2) the Cretaceous (K) contains the biggest oil reservoir, forming 78% of oil in the whole depression. Fig. 10(b) shows modeled gas accumulation data indicating: 1) only a little gas in the upper Tertiary (N_1j, $N_{1-2}k$); and 2) the Cretaceous (K) also contains the biggest gas reservoir, which accounts for 74% of gas in the whole depression, and the next is the lower Tertiary (E) which accounts for 15% of gas in the whole depression. These modeled results in each related formation coincide with actual exploration results.
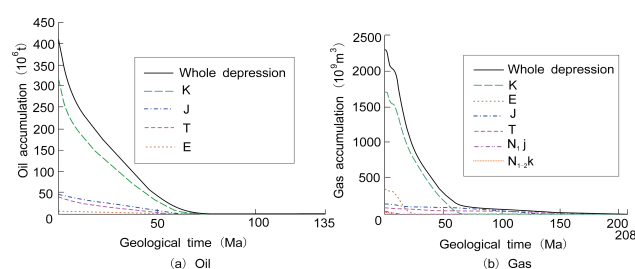

Figure 10
Oil and Gas Accumulation Histories of Each Related Formation in the Kuqa Depression

c. *The Modeled Oil and Gas Reservoirs Are Consistent with Actual Exploration Results*: A commercial oil flow has been discovered in the E (lower Tertiary) Yaha oilfield by comparing Fig. 11(a) with Fig. 3; commercial gas flows have been discovered in the K (Cretaceous) gas fields of Yaha, Yingmai7, Yangtake, Hongqi, Tiergen, Yudong, Kela2 and Dabei by comparing Fig. 11(b) with Fig. 3.

d. *Predictions from The Modeled Results*: From the modeling results shown in Fig. 11, we have the following predictions: some zones are prospective for further exploration, such as YM7-HQ2 and DW1 for oil (see Fig. 11(a)), and YT1-YT5, YX1 and DQ5 for gas (see Fig. 11(b)). This suggests that the lower Tertiary (E) and Cretaceous (K) will still form important exploration areas within the depression into the future.

The above four findings prove the validity, feasibility and practicality of the numerical method to a certain extent.
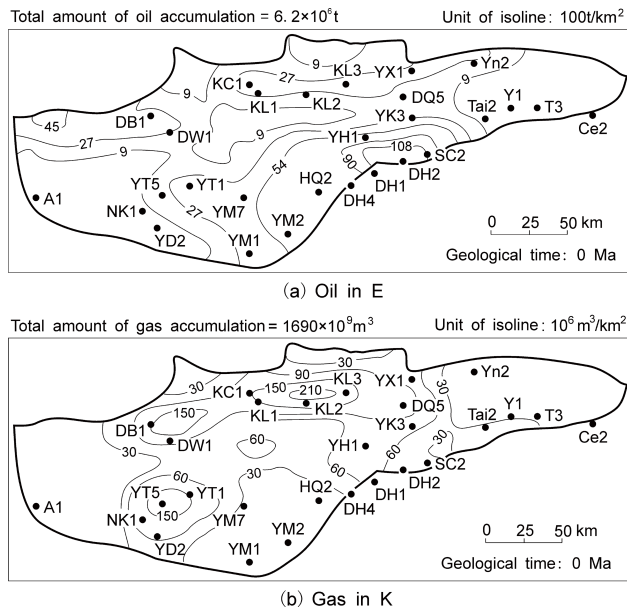
Figure 11
At 0 Ma (a) Cumulative Oil Accumulation in E (the lower Tertiary) and (b) Cumulative Gas Accumulation in K (the Cretaceous)

CONCLUSIONS

From the implementation, simulations, and case studies using the proposed finite volume method for modeling 3-D 3-phase secondary migration of oil and gas, we can draw the following conclusions:

1) The 3-D 3-phase (water, oil, gas) black-oil model, usually used in reservoir simulations, has been modified and applied to basin modeling as a new simulator for hydrocarbon secondary migration. Since the filtration environment and the solutions of basin modeling are much more complicated and difficult than those of reservoir simulations, we have to use several special processing modifications to account for variable simulation ranges, very long simulation times, initial conditions, natural sources and sinks, and reservoir gridcells.

2) The finite volume method with perpendicular bisection (PEBI) gridding is not only easy to implement, but also very flexible in dealing with various types of gridcells, irregular geometry, and various boundary conditions. Its advantages have now been demonstrated in the application of both reservoir simulations and basin modeling.

3) To ensure the stability and convergence of numerical solutions, the fully implicit (both implicit pressure and implicit saturation) formulation should be used, and gives much more accurate results than the IMPES (implicit pressure and explicit saturation) formulation. Moreover, it is vital for properly choosing the simulation timestep, and the maximum number of iterations for the Newton and ORTHOMIN methods.

4) Geologically speaking, our simulations concerning the Kuqa Depression agree with actual exploration data, which proves the proposed method is accurate and feasible. Moreover, some prospects predicted by the current modeling have been proved by recent exploration[33].

REFERENCES

[1] Shi, G. R., Li, H. F., Wang, S. M., Guo, Q. L., Shi, R. M., & Li, P. (1989). 1-D basin modeling system BAS1. *Petroleum Exploration and Development, 16*(6), 1-11. (in Chinese with English abstract)

[2] Welte, D. H., & Yükler, M. A. (1981). Petroleum origin and accumulation in basin evolution — A quantitative model. *AAPG Bulletin, 65*(8), 1387-1396.

[3] Yükler, M. A., Cornford, C., & Welte, D. H. (1978). One-dimensional model to simulate geologic, hydrodynamic and thermodynamic development of a sedimentary basin. *Geologische Rundschau, 67*(3), 960-979.

[4] Noureddine, Y., Schaefer, R. S., & Littke, R. (2001). Petroleum generation and accumulation in the Berkine basin, eastern Algeria. *AAPG Bulletin, 85*(8), 1439-1467.

[5] Shi, G. R., Guo, Q. L., Mi, S. Y., Zhang, Q. C., & Yang Q. L. (1996). Basin integrated modeling system BASIMS. *Acta Petrolei Sinica, 17*(1), 1-9. (in Chinese with English abstract)

[6] Ungerer P., Burrus, J., Doligez, B., Chenet, P. Y., & Bessis F. (1990). Basin evaluation by integrated two-dimensional modeling of heat transfer, fluid flow, hydrocarbon generation, and migration. *AAPG Bulletin, 74*(3), 309-335.

[7] Fugl, A. W., & Meshri I. D. (1998). 3-D modeling for migration and accumulation of hydrocarbons in the Danish Central Graben, North Sea. *AAPG Bulletin, 82*(3), 1916.

[8] Gonçalvès, J., Violette, S., Guillocheau, F., Robin, C., Pagel, M., Bruel, D., de Marsily, G., & Ledoux, E. (2004). Contribution of a three-dimensional regional scale basin model to the study of the past fluid flow evolution and the present hydrology of the Paris basin, France. *Basin Research, 16*(4), 569-586.

[9] Nielsen, S. B., & Gallagher, K. (1999). Efficient sampling of 3-D basin modelling scenarios. *AAPG Bulletin, 83*(8), 1330.

[10] Schneider, F., & Wolf, S. (2000). Quantitative HC potential evaluation using 3D basin modeling: application to Franklin structure, Central Grabben, North Sea, U. K. *Marine and Petroleum Geology, 17*(7), 841-856.

[11] Hantschel, T., & Kauerauf, A. I. (2009). *Fundamentals of Basin Modeling and Petroleum Systems Modeling*. Berlin, Germany: Springer-Verlag.

[12] Mello, U. T., Rodrigues, J. R. P., & Rossa, A. L. (2009). A control-volume finite-element method for three-dimensional multiphase basin modeling. *Marine and Petroleum Geology, 26*(4), 504-518.

[13] England, W. A., Mackenzie, A. S., Mann, D. M., & Quigley, T. M. (1987). The Movement and entrapment of petroleum fluids in the subsurface. *J. the Geological Society (London),*

144(2), 327-347.

[14] Thomas, C. W. (1982). *Principles of Hydrocarbon Reservoir Simulation*. Boston, USA: International Human Resources Development Corporation.

[15] Shi, G. R. (2008). Basin modeling in the Kuqa Depression of the Tarim Basin (Western China): A fully temperature-dependent model of overpressure history. *Mathematical Geosciences, 40*(1), 47-62.

[16] Smith, J. E. (1971). The dynamics of shale compaction and evolution in pore-fluid pressures. *Mathematical Geology. 3*(3), 239-263.

[17] Barcilon, V., & Richter, F. M. (1986). Non-linear waves in compacting media. *J. Fluid Mechanics, 164*, 429-448.

[18] Fowler, A. C., & Yang, X. S. (2002). Loading and unloading of sedimentary basins: the effect of rheological hysteresis. *J. Geophysical Research-Solid Earth, 107*(B4, 2058), doi: 10.1029/2001JB000389.

[19] Lerche, I. (1990). *Basin Analysis Quantitative Methods, Volume 1*. San Diego, CA, USA: Academic Press Inc.

[20] Matthäi, S. K., Aydin, A., Pollard, D. D., & Roberts, S. (1998). Numerical simulation of deviation from radial drawdown in a faulted sandstone reservoir with joints and zones of deformation bands. In *Faulting, Fault Sealing and Fluid Flow in Hydrocarbon Reservoirs, Geol. Soc. Spec. Publ. 147* (eds. G. Jones, Q. J. Fisher, R. J. Knipe), pp. 157-191. London, UK: Elsevier.

[21] Taylor, W. L., Pollard, D. D., & Aydin A. (1999). Fluid flow in discrete joint sets: field observations and numerical simulations. *J. Geophysical Research-Solid Earth, 104*(B12), 28983-29006.

[22] Taylor, W. L., & Pollard, D. D. (2000). Estimation of in situ permeability of deformation bands in porous sandstone, Valley of Fire, Nevada. *Water Resources Research, 36*(9), 2595-2606.

[23] Jourde, H., Flodin, E. A., Aydin, A., Durlofsky, L. J., & Wen, X. H. (2002). Computing permeability of fault zones in eolian sandstone from outcrop measurements. *AAPG Bulletin, 86*(7), 1187-1200.

[24] Shipton, Z. K., Evans, J. P., Robeson, K. R., Forster, C. B., & Snelgrove S. (2002). Structural heterogeneity and permeability in faulted eolian sandstone, implications for subsurface modeling of faults. *AAPG Bulletin, 86*(5), 863-883.

[25] Forsyth, P. A. (1989). A control volume finite element method for local mesh refinement. *SPE of AIME, 18415*, 85-96.

[26] Heinemann, Z. E., Brand, C., Munca, M., & Chen, Y. M. (1989). Modeling reservoir geometry with irregular grids. *SPE of AIME, 18412*, 37-54.

[27] Mishev, I. D. (1998). Finite volume methods on Voronoi meshes. *Numerical Methods for Partial Differential Equations, 14*(2), 193-212.

[28] Rozon, B. J. (1989). A generalized finite volume discretization method for reservoir simulation. *SPE of AIME, 18414*, 71-84.

[29] Bertiger, W. I., & Kelsey, F. J. (1985). Inexact adaptive Newton methods. *SPE of AIME, 13501*, 49-60.

[30] Vinsome, P. K. W. (1976). Orthomin, an iterative method for solving sparse sets of simultaneous linear equations. *SPE of AIME, 5729*, 149-159.

[31] Aziz, K., & Settari, A. (2002). *Petroleum Reservoir Simulation*. Calgary, Canada: Blitzprint limited.

[32] Shi, G. R., Zhou, X. X., Zhang, G. Y., Shi, X. F., & Li, H. H. (2004). The use of artificial neural network analysis and multiple regression for trap quality evaluation: a case study of the Northern Kuqa Depression of Tarim Basin in western China. *Marine and Petroleum Geology, 21*(3), 411-420.

[33] Shi, G. R., Zhang, Q. C., Yang, X. S., & Mi, S. Y. (2010). Oil and gas assessment of the Kuqa Depression of Tarim Basin in western China by simple fluid flow models of primary and secondary migrations of hydrocarbons. *J. Petroleum Science and Engineering, 75*(1-2), 77-90.

[34] Ungerer, P., Bessis, F., Chénet, P. Y., Durand, Nogaret, B., E., Chiarelli, A., Oudin, J. L., & Perrin, J. F. (1984). Geological and geochemical models in oil exploration; principles and practical examples. In *Petroleum Geochemistry and Basin Evaluation, AAPG Bulletin, Memoir 35* (eds. G. Demaison and R. J. Murris), pp. 53-77.

[35] Lerche, I., Yarzab, R. F., & Kendall, C. G. ST. C. (1984). Determination of paleoheat flux from vitrinite reflectance data. *AAPG Bulletin, 68*(11), 1704-1717.

[36] Lerche, I. (1988). Inversion of multiple thermal indicators, quantitative methods of determining paleoheat flux and geological parameters. I. theoretical development for paleoheat flux. *Mathematical Geology, 20*(1), 1-36.

[37] Shi, G. R. (2009). A simplified dissolution-precipitation model of the smectite to illite transformation and its application. *J. Geophysical Research-Solid Earth, 114*(B10205), 13 PP., doi: 10.1029/2009JB006406.

[38] Pepper, A. S., & Corv, P. J. (1995). Simple kinetic models of petroleum formation. Part I, Oil and gas generation from kerogen. *Marine and Petroleum Geology, 12*(1995), 291-319.

[39] Pepper, A. S., & Dodd, T. A. (1995). Simple kinetic models of petroleum formation. Part П, Oil-gas cracking. *Marine and Petroleum Geology, 12*(3), 321-340.

[40] Nakayama, K. (1987). Hydrocarbon-expulsion model and its application to Niigata area, Japan. *AAPG Bulletin, 71*(7), 810-821.

[41] Okui, A., & Waples, D. W. (1993). Relative permeability and hydrocarbon expulsion from source rocks. In *Basin Modeling: Advances and Applications* (eds. A. G. Doré et al.), pp. 293-301. Amsterdam, Holland: Elsevier.

[42] Okui, A., Siebert, R. M., & Matsubayashi, H. (1998). Simulation of oil expulsion by 1-D and 2-D basin modeling — saturation threshold and relative permeabilities of source rock. In *Basin Modelling: Practice and Progress, Geol. Soc. Spec. Publ. 141* (eds. S. J. Düppenbecker and J. E. Iliffe), pp. 45-72. London, UK: Elsevier.

[43] Özkaya, I. (1991). Computer simulation of primary oil migration in Kuwait. *J. Petroleum Geology, 14*(1), 37-48.

[44] Pepper, A. S., & Corv, P. J. (1995). Simple kinetic models

of petroleum formation. Part Ⅲ, Modelling an open system. *Marine and Petroleum Geology, 12*(4), 417-452.

[45] Li, D. S., & Li, D. W. (2003). *Tectonic Types of Oil and Gas Basins in China, second ed*. Beijing, China: Petroleum Industry Press.

[46] Zhou, X. X., Zhang, G. Y., Li, H. H., Wang, H. J., & Jia, J. H. (2002). *Factors of Pool-forming of the Kuqa Petroleum System in the Tarim Basin*. Beijing, China: Petroleum Industry Press. (in Chinese)